
Projected-point-based Segmentation: A New Paradigm for LiDAR Point Cloud Segmentation

Shijie Li

University of Bonn
lishijie@iai.uni-bonn.de

Yun Liu

Nankai University
nk12csly@mail.nankai.edu.cn

Juergen Gall

University of Bonn
gall@iai.uni-bonn.de

Abstract

Most point-based semantic segmentation methods are designed for indoor scenarios, but many applications such as autonomous driving vehicles require accurate segmentation for outdoor scenarios. For this goal, light detection and ranging (LiDAR) sensors are often used to collect outdoor environmental data. The problem is that directly applying previous point-based segmentation methods to LiDAR point clouds usually leads to unsatisfactory results due to the domain gap between indoor and outdoor scenarios. To address such a domain gap, we propose a new paradigm, namely projected-point-based methods, to transform point-based methods to a suitable form for LiDAR point cloud segmentation by utilizing the characteristics of LiDAR point clouds. Specifically, we utilize the inherent ordered information of LiDAR points for point sampling and grouping, thus reducing unnecessary computation. All computations are carried out on the projected image, and there are only pointwise convolutions and matrix multiplication in projected-point-based methods. We compare projected-point-based methods with point-based methods on the challenging SemanticKITTI dataset, and experimental results demonstrate that projected-point-based methods achieve better accuracy than all baselines more efficiently. Even with a simple baseline architecture, projected-point-based methods perform favorably against previous state-of-the-art methods. The code will be released upon paper acceptance.

1 Introduction

Understanding the environment is essential for autonomous driving vehicles. For this goal, light detection and ranging (LiDAR) sensors are usually used and the semantic segmentation of the point clouds captured by LiDAR sensors is an essential step for autonomous vehicles. In recent years, several deep learning approaches have been proposed that operate on point clouds [14, 15, 18, 22]. These point-based methods perform very well for small-scale indoor scenarios where dense point clouds are generated by fusing data captured by RGB-D sensors. It was, however, shown in [1] that these methods do not perform well in terms of efficiency and accuracy for point clouds captured by a rotational LiDAR sensor in outdoor scenarios. This is due to two reasons. First, the computational cost of point-based methods increases with the total number of points in a point cloud and LiDAR point clouds for outdoor scenes are very large. Second, the density of LiDAR point clouds drops rapidly with the distance to the LiDAR sensor as shown in the top row of Fig. 1.

In this work, we address these issues and demonstrate that point-based methods can be reformulated such that they are suitable for LiDAR data. The core idea is that we make use of a projection of the

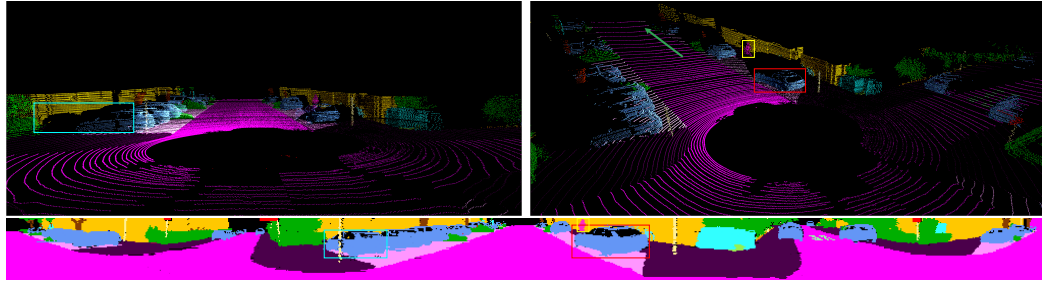


Figure 1: Due to the nature of LiDAR sensors, the captured 3D point cloud can be projected onto a plane. This means that neighboring points in 3D are also close in the projected plane, but neighbors in the projected plane can be far distant in 3D. Furthermore, the points become more sparse as the distance to the sensor increases (green arrow) while the points are dense in the projection. We highlight some objects by bounding boxes as an example. Best seen using the zoom function of a PDF viewer.

LiDAR point cloud as shown in the bottom row of Fig. 1. In contrast to methods [20, 21, 12] that apply 2D convolutions, we preserve the architectures and the operations of point-based methods.

Point-based methods comprise several steps that are repeated within the network architecture. These steps include the sampling of 3D points of the point cloud, grouping neighboring points for each sampled point, and computing a feature based on the grouped points. In this work, we show how these operations can be performed in the projected space and how these operations can be efficiently implemented. Although the operations are the same, the projection leads to significant differences. For instance, the sampled points are differently distributed as shown in Fig. 3. The sampled points of the projected-point version are actually better distributed than the sampled points of the point-based methods that oversample the sparse distant points in a LiDAR point cloud. We term the projected versions of point-based methods projected-point-based methods.

As examples, we use PointNet++ [15], SpiderCNN [23], and PointConv [22] as point-based approaches and convert them into projected-point-based methods. We evaluate them on the SemanticKITTI dataset [1], which is a large-scale dataset for semantic segmentation of LiDAR point clouds. For the three point-based methods, the projected-point-based methods reduce the runtime by factors between 300 and 400 and increase the mIoU by 58% - 68%.

In summary, we show in this works that

- point-based methods can be converted into projected-point-based methods for processing LiDAR point clouds,
- the converted point-based methods are more efficient and achieve a higher accuracy than the original point-based methods.

2 Related Work

In this section, we briefly review recent methods for LiDAR point cloud segmentation. Although CNN-based methods have achieved great success in 2D image segmentation, they cannot be directly applied to point cloud segmentation. This is because the point cloud is in an orderless structure and it is difficult to extract local features for 3D points. To handle this problem, permutation-invariant operations are adopted in PointNet [14] to aggregate information. However, the local information is not taken into consideration in PointNet [14], which leads to performance loss. This is addressed in PointNet++ [14] by gathering local information gradually. The gathering operations in PointNet [14] and PointNet++ [14] are pooling operations which ignore the relative position in the local area. SpiderCNN [23] models this information by a polynomial and achieves better performance. The distribution of 3D points is usually unbalanced, which provides informative clues for the recognition. PointConv [22] explicitly fuses density information into the architecture to improve model representation ability. PointCNN [11] proposes a is a generalization of typical CNNs to feature learning from point clouds. 3DMV [3] combines 2D and 3D features together for better predictions. Apart from directly processing 3D information, TangentConv [18] projects local points

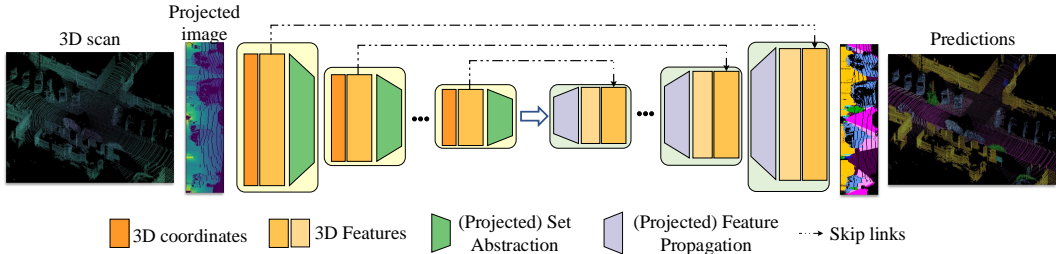


Figure 2: Overall architecture of PointNet++ or its projected-point-based version (P²Net++).

to a tangent plane and applies 2D convolutions on it. The above methods are mainly designed for small-scale scenes with a limited number of points, especially for indoor scenarios. Different from them, SPGraph [10] is more suitable for large-scale scenes by defining super-point to extract compact representation. However, these methods do not take the distribution characteristic of LiDAR point clouds into consideration and are thus suboptimal in both performance and efficiency.

Recently, there are some methods that convert the 3D point cloud to a 2D image according to the scan pattern of LiDAR sensors and then apply a 2D CNN on this 2D image. FuseSeg [9] combines color and spatial information to segment LiDAR point clouds. DeepTemporalSeg[4] proposes a temporally consistent method for LiDAR point cloud segmentation. SqueezeSeg methods [20, 21] adopt SqueezeNet [7] as the backbone and use a conditional random field (CRF) as post-processing. PointSeg [19] adopts a similar architecture as SqueezeNet [7] but uses dilation convolution to keep more spatial information. Based on SqueezeSeg, RangeNet++ [12] replaces the backbone with Darknet [16] and designs a k -Nearest-Neighbor (k -NN) search as its post-processing. Ideally, only nearby information should be utilized for label prediction. However, the nearby points in the projected image may be far away in the 3D space as shown in Fig. 1. In the proposed projected-point-based methods, 3D neighbor points are used instead of 2D ones to avoid this problem.

3 Projected PointNet

In order to show how a network operating on Lidar points can be converted into a projected-point-based method, we use PointNet++ [15] as an example. In Section 3.3, we discuss the projected-point-based versions of two other point-based networks, namely SpiderCNN [23] and PointConv [22]. Before we discuss our approach in Section 3.2, we briefly discuss the main operations of PointNet++.

3.1 Review of PointNet++

We choose PointNet++ [15] as an example since it is very popular and has been used as the baseline in many works. The pipeline of PointNet++ is shown in Fig. 2. PointNet++ consists of so-called Set Abstraction modules and Feature Propagation modules as shown in Fig. 2. The Set Abstraction module comprises a sampling layer, a grouping layer, and a PointNet layer. The sampling layer chooses a subset from the input point set, which defines the centroids of local regions. Fig. 3 shows the sampled points. The grouping layer groups the neighboring points of each centroid, which forms a local region. The PointNet layer computes a feature vector based on the neighboring points using a multilayer perceptron (MLP) and max pooling. While the set abstraction modules subsample the original point set, the feature propagation modules recover the original point set by distance based interpolation:

$$f^{(j)}(x) = \frac{\sum_{i=1}^k w_i(x) f_i^{(j)}}{\sum_{i=1}^k w_i(x)} \quad \text{where} \quad w_i(x) = \frac{1}{d(x, x_i)^p}, j = 1, \dots, C, \quad (1)$$

where f is a point-wise feature and $d(x_i, x_j)$ is the distance between point x_i and x_j .

3.2 Projected PointNet++

To convert PointNet++ into a projected-point-based method, we will not change the architecture, but we need to convert the Set Abstraction and the Feature Propagation module into projected versions as shown in Fig. 2. As input, we use the projected LiDAR point cloud as it has been proposed in

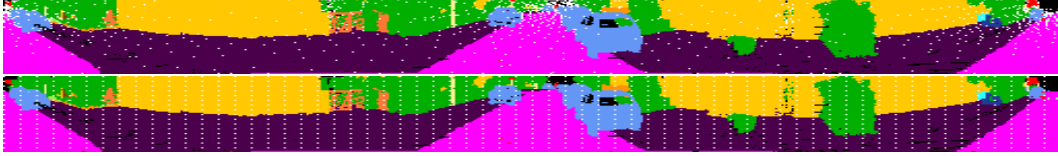


Figure 3: Comparison of the sampling methods in PointNet++ (top) and projected PointNet++ (bottom). 1024 points are sampled from the LiDAR point cloud. For better visualization, we show the 2D projected image with white points denoting the sampled points. PointNet++ only samples a few points for close objects like cars and most sampled points lie on the distant region where the real distribution of points is sparse, making it unable to reveal the real data distribution.

[20]. We will first describe the projected sampling layer (Section 3.2.1), the projected grouping layer (Section 3.2.2), and the projected PointNet layer (Section 3.2.3) of the projected Set Abstraction module and then the projected Feature Propagation (Section 3.2.4).

3.2.1 Projected Sampling Layer

PointNet++ [15] uses farthest point sampling to sample a subset of 3D points. It is designed to maximize the distance between sampled points that are thus uniformly scattered in the 3D space. However, the real distribution of LiDAR points is not uniform and becomes sparse as the distance to the sensor increases as shown in Fig. 1. This mismatch harms the performance when applying farthest point sampling to LiDAR points, as shown in Fig. 3. Furthermore, the computational complexity of FPS is $\mathcal{O}(N \log N)$ where N is the number of 3D points [8]. This makes the approach highly inefficient for large point clouds which are common for Lidar sensors. Therefore, farthest point sampling is suboptimal for LiDAR point cloud segmentation in terms of both effectiveness and efficiency. To address this problem, we propose to uniformly sample the 3D points from the projected point cloud as shown in Fig. 3. This has the advantage that we sample rays instead of points, which means that the distance between the sampled points is larger if they are farther away from the sensor. Hence the distribution of sampled points accords with the original point cloud. Another benefit is that we can use a 2D grid structure for sampling such that the computational complexity becomes $\mathcal{O}(M)$ where $M = H' \times W'$ is the number of sampled points and $M \ll N$.

3.2.2 Projected Grouping Layer

For grouping neighboring 3D points, PointNet++ uses a ball query to obtain for each sampled point all points that are within a given distance. While a naive implementation has the complexity of $\mathcal{O}(MN)$, more efficient implementations reduce it using data structures like k-d trees or octrees [2]. This, however, increases memory requirements. In order to make the grouping of PointNet++ [15] much more efficient, we search neighboring rays first and then exclude the points that are too far away from the sampled point. We obtain the neighboring rays by taking the $k \times k$ neighbors in the projected point cloud as shown in Fig. 4. The parameter k provides a trade-off between accuracy and runtime as we will show in the experiments. For each of the k^2 points, we obtain the 3D points and subtract the 3D position of the sampled point to convert the points from global coordinates to local coordinates as in PointNet++. We then compute the norm of each point, *i.e.*, the 3D distance to the sampled point, and mask all points that are within a given distance. The complexity of this operation is $\mathcal{O}(Mk^2)$ where $k^2 \ll \log N$. A comparison between this grouping strategy and the grouping in PointNet++ is displayed in Fig. 4.

Fig. 5 illustrates how projected sampling and grouping are efficiently implemented in a network. Given the input $\mathbb{R}^{(C+3) \times H \times W}$, where C is the number of feature channels, which are concatenated with the 3D coordinates ($C + 3$), the unfold operations uniformly samples $H' \times W'$ points as discussed in Section 3.2.1 and copies the corresponding $k \times k$ neighborhood for each sampled point $m \in H' \times W'$. This yields the tensor $F_{in} \in \mathbb{R}^{(C+3) \times k^2 \times H' \times W'}$. For each sampled point, we then subtract the 3D coordinate of the sampled point from the coordinates of the corresponding k^2 neighboring points. We finally compute the distance map $\mathbb{R}^{k^2 \times H' \times W'}$ and the binary neighborhood mask $\{0, 1\}^{k^2 \times H' \times W'}$, which is 1 if a point is within the radius of a sampled point. The neighborhood mask defines the grouping for each sampled point.

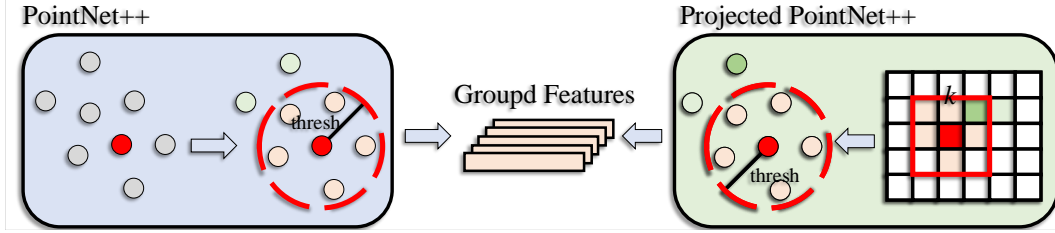


Figure 4: Comparison of the projected grouping layer (right) with the original one in PointNet++ [15] (left). PointNet++ uses a ball query to obtain for each sampled point (red) all neighboring points (orange) within a certain radius. In contrast, our method searches first the $k \times k$ neighboring rays and then we discard the points that are outside the radius (dark green point).

At this step, we directly compute the inverse distance map, which will be used in the Projected Feature Propagation module described in the next section, and the inverse density map as described in [22]. The latter will be needed for converting PointConv [22] into a projected-point-based method.

3.2.3 Projected PointNet Layer

The PointNet layer in PointNet++ uses max pooling and an MLP. Given $F_{in} \in \mathbb{R}^{(C+3) \times k^2 \times H' \times W'}$ after the unfold operation and the neighborhood mask, the projected point net layer can thus be formulated as

$$F_{out} = Pooling(MLP(F_{in} \otimes \mathcal{M})). \quad (2)$$

The symbol \otimes denotes element-wise multiplication and \mathcal{M} is the neighborhood mask, which has been duplicated $(C + 3)$ -times to have the same size as F_{in} . Fig. 7a illustrates this operation.

3.2.4 Projected Feature Propagation Module

As described in Section 3.1 and illustrated in Fig. 2, the feature propagation modules recover the original point set by distance based interpolation Equ. (1). Since our sampled points are uniformly distributed on the projected image, this can be very efficiently implemented. The sampled points are first set back to its original positions. The distance based interpolation (Inp) is then applied as in Equ. (1) using the precomputed inverse distance map \hat{D} . As illustrated in Fig. 2, there are skip connections between the blocks. The interpolated features $Inp(F_{in}, \hat{D})$ are thus concatenated with the point features from the corresponding set abstraction module (\hat{F}) and fed into an MLP, i.e.,

$$F_{out} = MLP(Concat(Inp(F_{in}, \hat{D}), \hat{F})) \quad (3)$$

The projected version of the Feature Propagation module is illustrated in Fig. 6.

3.3 Projected SpiderCNN and PointConv

So far we discussed how PointNet++ [15] can be converted into a projected-point-based method, but the approach can be applied to other point-based networks as well. In this section, we therefore briefly describe how two other networks, namely SpiderCNN [23] and PointConv [22], are converted

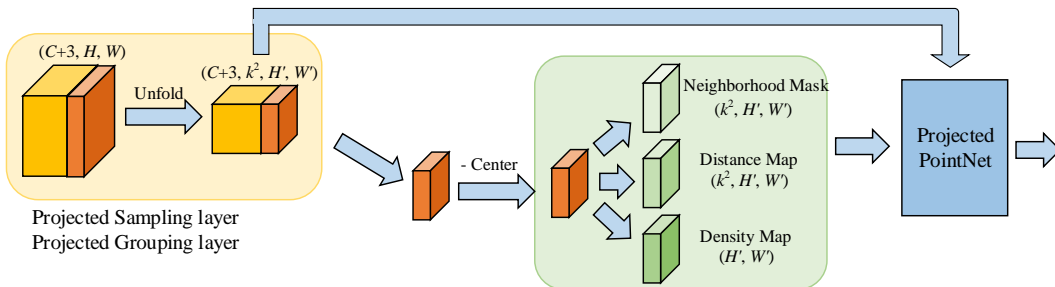


Figure 5: Illustration of the projected version of the Set Abstraction module.

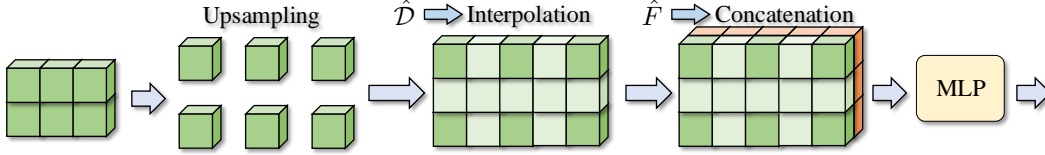


Figure 6: Illustration of the projected feature propagation module.

into projected-point-based methods. Fig. 7 illustrates the differences between the projected versions of PointNet++, SpiderCNN, and PointConv.

Projected SpiderCNN (PSCNN) can be viewed as a ‘soft’ version of P^2 Net++ because it weights each point feature according to its relative position to the corresponding sampled point. Instead of using a neighborhood mask, it computes the weight for each point. In our case, the operations are performed for the $k \times k$ neighborhood. The operations of the set abstraction in PSCNN are thus defined by

$$F_{out} = MLP_{out}(MLP_{in}(F_{in}) \boxtimes WeightNet(\mathcal{P})) \quad (4)$$

where the symbol \boxtimes denotes matrix multiplication, and \mathcal{P} denotes the unfolded 3D coordinates after subtracting the 3D coordinates of the corresponding sampled point as shown in Fig. 5. Here, we omit the dimensions which are shown in Fig. 7c. For feature propagation, PSCNN follows Equ. (3) and the main difference is that PSCNN applies Equ. (4) on the interpolated features.

Projected PointConv (P^2 Conv) uses the point density as additional information. The green branch in Fig. 7d therefore takes the inverse density map \mathcal{D} from Fig. 5 as in input. The operations of the set abstraction in P^2 Conv are defined by

$$F_{out} = MLP_{out}((MLP_{in}(F_{in}) \otimes DensityNet(\mathcal{D})) \boxtimes WeightNet(\mathcal{P})). \quad (5)$$

Similar to PSCNN, P^2 Conv follows Equ. (3) for feature propagation, but it applies Equ. (5) on the interpolated features.

These examples show that point-based methods can be easily converted into projected-point-based methods. Since there are only some pointwise convolutions and multiplication operations, projected-point-based methods are very efficient and allow them to process several LiDAR scans per second.

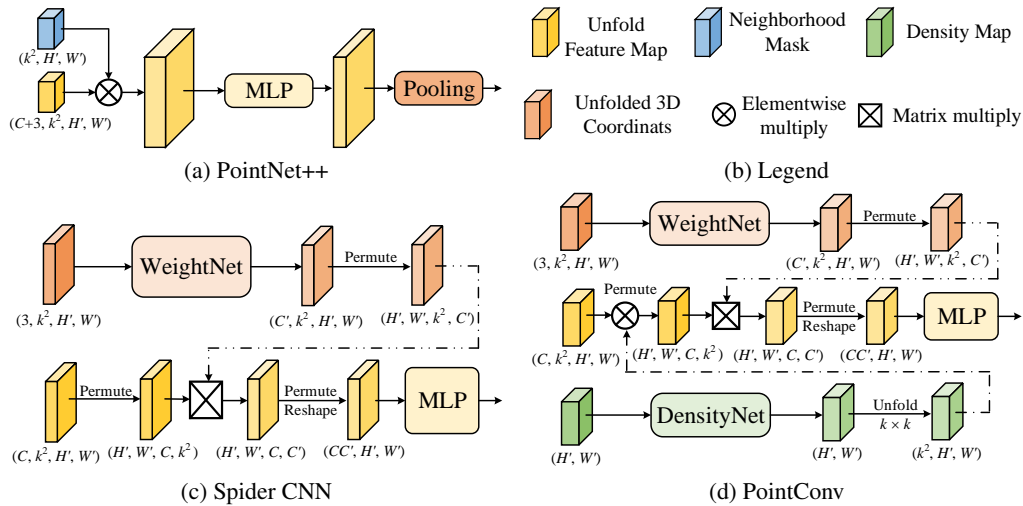


Figure 7: Projected versions of the set abstraction module for PointNet++ [15], SpiderCNN [23], and PointConv [22]. For the dimension mismatch in the element-wise operations, we omit the broadcasting mechanism because it is the default operation in modern deep learning frameworks like PyTorch [13]. We also omit MLP_{in} from Equ. (4) and Equ. (5).

4 Discussion of Projected-point-based and Projected-based Methods

Although both projected-point-based and projected-based methods use a projection, the main difference between them is that projected-point-based methods learn deep features from 3D-neighboring points as 3D point-based methods, while projected-based methods apply 2D convolutions to the projected 2D image neglecting 3D spatial relations. In this work, we show how point-based methods can be converted into projected-point-based methods without changing the architecture design and principles. This potentially allows us to leverage 3D point-based methods and projected-based methods in the future where 2D convolutions and operations over a set of points are combined. Therefore, the proposed projected-point-based methods open a new perspective for LiDAR point cloud segmentation, which shows promising results as discussed in the next section.

5 Experiments

5.1 Experimental Setup

We use the SemanticKITTI dataset [1] to evaluate our method. SemanticKITTI provides pixel-wise semantic labels for the entire KITTI Odometry Benchmark [6]. We adopt its training set for training, its validation set for ablation study, and its test set for the comparison with state-of-the-art methods. To evaluate each segmentation method, we use the well-known mean intersection over union (mIoU) metric [5] over all classes. For a fair comparison, all experiments are performed with a single GPU.

5.2 Ablation Study

To better understand the projected-point-based segmentation, we first explore the influence of the size k of the 2D search region in the projected grouping layer. Here, we evaluate projected PointNet++ (P²Net++) with an input resolution of 64×512 . The results are shown in the left of Tab. 1. We can see that the performance improves and the speed slows down with the search size k increasing. However, the improvement from $k = 5$ to $k = 7$ is not as large as that from $k = 3$ to $k = 5$, which suggests the local region with $k = 5$ has already included most important neighboring points. Considering the trade-off between effectiveness and efficiency, we set $k = 5$ in the following experiments.

Then, we evaluate the effect of different input resolutions, and we summarize the results in Tab. 1. We can observe that increasing the input resolution from 64×512 to 64×1024 can slightly improve performance but the cost is more computational load. However, when the resolution changes from 64×1024 to 64×2048 , the performance degrades dramatically. Maybe this is because when increasing the input resolution, the search size k is kept the same, which leads to a smaller receptive field. For a good trade-off between effectiveness and efficiency, we set the input resolution to 64×512 if not mentioned.

Finally, we compare the original models with their projected version. The three baseline methods are PointNet++ [15], SpiderCNN [23] and PointConv [22]. We display the results in Tab. 2. We can see that the projected-point-based methods achieve much better performance than the original baselines. The improvement is about 10% for all baselines in terms of both accuracy and mIoU. For SpiderCNN [23] and PointConv [22], the mIoU is even improved by about 15%. These results prove the effectiveness of projected-point-based methods. We show some visualization in Fig. 8.

k	Acc	mIoU	Scans/s	Resolution	Acc	mIoU	Scans/s
3	71.4	26.8	38.2	64×512	74.7	30.7	30.0
5	74.7	30.7	30.0	64×1024	77.4	31.3	17.2
7	76.2	31.9	23.7	64×2048	75.2	25.7	9.4

Table 1: Effect of different search sizes k (left) and different input resolutions (right).

	PointNet++ [15]	P ² Net++	SCNN [23]	PSCNN	PCConv [22]	P ² Conv
Acc	64.6	74.7	70.3	81.5	72.5	82.5
mIoU	19.4	30.7	21.8	36.8	23.2	37.6
Scans/sec	0.1	30.0	0.04	12.9	0.03	12.2

Table 2: Comparison with the original baseline methods.

Approach	car	bicycle	motorcycle	truck	other-vehicle	person	bicyclist	motorcyclist	road	parking	sidewalk	other-ground	building	fence	vegetation	trunk	terrain	pole	traffic-sign	mIoU	Scans/sec
Pointnet [14]	46.3	1.3	0.3	0.1	0.8	0.2	0.2	0.0	61.6	15.8	35.7	1.4	41.4	12.9	31.0	4.6	17.6	2.4	3.7	14.6	2
Pointnet++ [15]	53.7	1.9	0.2	0.9	0.2	0.9	1.0	0.0	72.0	18.7	41.8	5.6	62.3	16.9	46.5	13.8	30.0	6.0	8.9	20.1	0.1
SPGraph [10]	68.3	0.9	4.5	0.9	0.8	1.0	6.0	0.0	49.5	1.7	24.2	0.3	68.2	22.5	59.2	27.2	17.0	18.3	10.5	20.0	0.2
SPLATNet [17]	66.6	0.0	0.0	0.0	0.0	0.0	0.0	0.0	70.4	0.8	41.5	0.0	68.7	27.8	72.3	35.9	35.8	13.8	0.0	22.8	1
TangentConv [18]	86.8	1.3	12.7	11.6	10.2	17.1	20.2	0.5	82.9	15.2	61.7	9.0	82.8	44.2	75.5	42.5	55.5	30.2	22.2	35.9	0.3
P ² Net++	73.3	13.0	5.4	11.8	8.3	6.4	15.5	2.1	86.3	40.1	60.1	7.2	61.7	32.1	55.8	13.1	51.6	4.2	14.7	29.6	30.0
P ² Net++*	78.9	13.4	6.2	12.0	8.5	7.2	18.7	2.2	86.4	40.9	60.7	6.7	65.9	33.8	58.3	14.6	52.8	5.6	19.8	31.2	29.4
PSCNN	79.8	19.8	11.2	15.8	14.3	15.1	20.5	8.8	87.1	41.8	64.7	8.7	72.2	37.9	68.0	28.4	58.0	13.1	31.3	36.7	12.9
PSCNN*	85.9	20.8	13.2	16.2	14.8	16.9	28.8	9.3	87.1	42.4	65.3	8.5	76.9	40.8	71.1	33.3	59.5	21.1	37.7	39.5	12.6
P ² Conv	79.5	19.0	12.7	13.8	10.7	14.9	18.2	5.8	87.8	46.6	66.6	7.3	73.2	40.1	69.4	30.9	59.3	14.1	32.1	36.9	12.2
P ² Conv*	85.6	20.4	14.4	14.4	11.5	16.9	24.9	5.9	87.8	47.5	67.3	7.3	77.9	43.4	72.5	36.5	60.8	22.8	38.2	39.8	12.1

Table 3: Comparison with state-of-the-art methods. The symbol * means using k -NN post-processing.

5.3 Comparison with State-of-the-art methods

In this part, we compare our projected-point-based methods with previous state-of-the-art methods on the SemanticKITTI test set. The results are shown in Tab. 3. We can see that even without the best setting (large search size and input resolution) or modern architecture (we use a simple encoder-decoder architecture without adjustment), projected-point-based methods perform favorably against previous state-of-the-art methods. Projected-point-based methods are also much faster than other methods. This proves the effectiveness and efficiency of our design. Another advantage of our design is that it can utilize the highly efficient k -NN [12] as post-processing to further improve performance. k -NN post-processing can boost the mIoU by about 2% to 3%. We also find that most point-based methods can hardly detect small objects (*e.g.*, near 0 mIoU for the classes of bicycle, truck, and motorcyclist), but projected-point-based methods can successfully detect small objects.

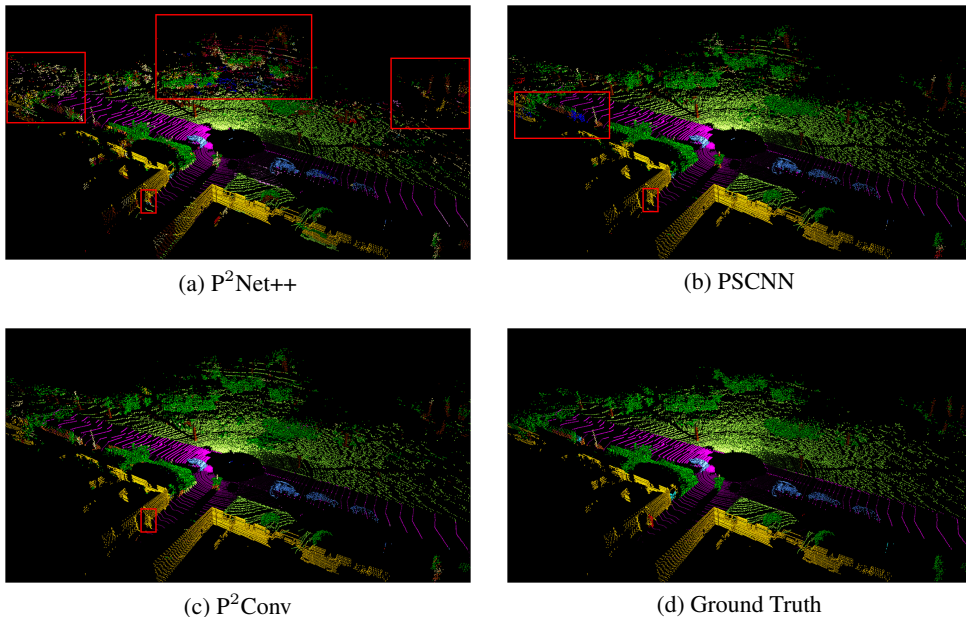


Figure 8: Qualitative visualization. We highlight wrong predictions using red boxes. P²Net++ gets bad predictions for distant scenes due to the weak aggregation capability of pooling operations. P²Conv achieves better results than PSCNN, which proves the effectiveness of density information.

6 Conclusion

In this paper, we propose a new paradigm to convert point-based methods to projected-point-based methods for LiDAR point cloud segmentation by utilizing the distribution characteristic of LiDAR points. We evaluate our method on three point-based baselines. The experimental results demonstrate that projected-point-based methods achieve much better segmentation accuracy and efficiency than the original point-based methods consistently. Even with the simplest architecture, the converted model performs favorably against previous state-of-the-art methods. In the future, we plan to design new architectures based on projected-point-based methods for further improvement.

Broader Impact Discussion

This paper opens a new perspective for LiDAR point cloud segmentation by converting point-based segmentation methods to projected-point-based methods. This work can be applied to autonomous driving vehicles for environment understanding where LiDAR sensors are often used to collect environmental data. This work has no obvious harm to society, and it is not our original intention if this work is used for some bad purposes as other computer vision techniques.

References

- [1] J. Behley, M. Garbade, A. Milioto, J. Quenzel, S. Behnke, C. Stachniss, and J. Gall. SemanticKITTI: A dataset for semantic scene understanding of LiDAR sequences. In *IEEE International Conference on Computer Vision*, pages 9297–9307, 2019.
- [2] J. Behley, V. Steinhage, and A. B. Cremers. Efficient radius neighbor search in three-dimensional point clouds. In *IEEE International Conference on Robotics and Automation*, pages 3625–3630, 2015.
- [3] A. Dai and M. Nießner. 3dmv: Joint 3d-multi-view prediction for 3d semantic scene segmentation. In *Proceedings of the European Conference on Computer Vision (ECCV)*, pages 452–468, 2018.
- [4] A. Dewan and W. Burgard. Deeptemporalseg: Temporally consistent semantic segmentation of 3d lidar scans. *arXiv preprint arXiv:1906.06962*, 2019.
- [5] M. Everingham, S. A. Eslami, L. Van Gool, C. K. Williams, J. Winn, and A. Zisserman. The PASCAL visual object classes challenge: A retrospective. *International Journal of Computer Vision*, 111(1):98–136, 2015.
- [6] A. Geiger, P. Lenz, and R. Urtasun. Are we ready for autonomous driving? The KITTI vision benchmark suite. In *IEEE Conference on Computer Vision and Pattern Recognition*, pages 3354–3361. IEEE, 2012.
- [7] F. N. Iandola, S. Han, M. W. Moskewicz, K. Ashraf, W. J. Dally, and K. Keutzer. SqueezeNet: AlexNet-level accuracy with 50x fewer parameters and <0.5MB model size. *arXiv preprint arXiv:1602.07360*, 2016.
- [8] P. Kamousi, S. Lazard, A. Maheshwari, and S. Wuhler. Analysis of farthest point sampling for approximating geodesics in a graph. *Computational Geometry*, 57:1 – 7, 2016.
- [9] G. Krispel, M. Opitz, G. Waltner, H. Possegger, and H. Bischof. Fuseseg: Lidar point cloud segmentation fusing multi-modal data. In *The IEEE Winter Conference on Applications of Computer Vision*, pages 1874–1883, 2020.
- [10] L. Landrieu and M. Simonovsky. Large-scale point cloud semantic segmentation with superpoint graphs. In *IEEE Conference on Computer Vision and Pattern Recognition*, pages 4558–4567, 2018.
- [11] Y. Li, R. Bu, M. Sun, W. Wu, X. Di, and B. Chen. Pointcnn: Convolution on x-transformed points. In *Advances in neural information processing systems*, pages 820–830, 2018.
- [12] A. Milioto, I. Vizzo, J. Behley, and C. Stachniss. RangeNet++: Fast and accurate LiDAR semantic segmentation. In *IEEE/RSJ International Conference on Intelligent Robots and Systems*, 2019.
- [13] A. Paszke, S. Gross, F. Massa, A. Lerer, J. Bradbury, G. Chanan, T. Killeen, Z. Lin, N. Gimelshein, L. Antiga, et al. PyTorch: An imperative style, high-performance deep learning library. In *Advances in Neural Information Processing Systems*, pages 8024–8035, 2019.
- [14] C. R. Qi, H. Su, K. Mo, and L. J. Guibas. PointNet: Deep learning on point sets for 3d classification and segmentation. In *IEEE Conference on Computer Vision and Pattern Recognition*, pages 652–660, 2017.
- [15] C. R. Qi, L. Yi, H. Su, and L. J. Guibas. PointNet++: Deep hierarchical feature learning on point sets in a metric space. In *Advances in Neural Information Processing Systems*, pages 5099–5108, 2017.
- [16] J. Redmon and A. Farhadi. YOLOv3: An incremental improvement. *arXiv preprint arXiv:1804.02767*, 2018.
- [17] H. Su, V. Jampani, D. Sun, S. Maji, E. Kalogerakis, M.-H. Yang, and J. Kautz. SPLATNet: Sparse lattice networks for point cloud processing. In *IEEE Conference on Computer Vision and Pattern Recognition*, pages 2530–2539, 2018.
- [18] M. Tatarchenko, J. Park, V. Koltun, and Q.-Y. Zhou. Tangent convolutions for dense prediction in 3D. In *IEEE Conference on Computer Vision and Pattern Recognition*, pages 3887–3896, 2018.
- [19] Y. Wang, T. Shi, P. Yun, L. Tai, and M. Liu. Pointseg: Real-time semantic segmentation based on 3d lidar point cloud. *arXiv preprint arXiv:1807.06288*, 2018.
- [20] B. Wu, A. Wan, X. Yue, and K. Keutzer. SqueezeSeg: Convolutional neural nets with recurrent CRF for real-time road-object segmentation from 3D LiDAR point cloud. In *IEEE International Conference on Robotics and Automation*, pages 1887–1893. IEEE, 2018.
- [21] B. Wu, X. Zhou, S. Zhao, X. Yue, and K. Keutzer. SqueezeSegV2: Improved model structure and unsupervised domain adaptation for road-object segmentation from a LiDAR point cloud. In *International Conference on Robotics and Automation*, pages 4376–4382. IEEE, 2019.
- [22] W. Wu, Z. Qi, and L. Fuxin. PointConv: Deep convolutional networks on 3D point clouds. In *IEEE Conference on Computer Vision and Pattern Recognition*, pages 9621–9630, 2019.
- [23] Y. Xu, T. Fan, M. Xu, L. Zeng, and Y. Qiao. SpiderCNN: Deep learning on point sets with parameterized convolutional filters. In *European Conference on Computer Vision*, pages 87–102, 2018.